

## ANTHROPOLOGY

# Role of climate in the rise and fall of the Neo-Assyrian Empire

Ashish Sinha<sup>1\*</sup>, Gayatri Kathayat<sup>2†\*</sup>, Harvey Weiss<sup>3,4†</sup>, Hanying Li<sup>2†</sup>, Hai Cheng<sup>2,5</sup>, Justin Reuter<sup>6</sup>, Adam W. Schneider<sup>7</sup>, Max Berkelhammer<sup>8</sup>, Selim F. Adali<sup>9</sup>, Lowell D. Stott<sup>10</sup>, R. Lawrence Edwards<sup>5</sup>

Northern Iraq was the political and economic center of the Neo-Assyrian Empire (c. 912 to 609 BCE)—the largest and most powerful empire of its time. After more than two centuries of regional dominance, the Neo-Assyrian state plummeted from its zenith (c. 670 BCE) to complete political collapse (c. 615 to 609 BCE). Earlier explanations for the Assyrian collapse focused on the roles of internal politico-economic conflicts, territorial overextension, and military defeat. Here, we present a high-resolution and precisely dated speleothem record of climate change from the Kuna Ba cave in northern Iraq, which suggests that the empire's rise occurred during a two-centuries-long interval of anomalously wet climate in the context of the past 4000 years, while megadroughts during the early-mid seventh century BCE, as severe as recent droughts in the region but lasting for decades, triggered a decline in Assyria's agrarian productivity and thus contributed to its eventual political and economic collapse.

## INTRODUCTION

Based in the floodplain of the Tigris River in ancient northern Mesopotamia (now northern Iraq), the Neo-Assyrian Empire emerged during the 10th century BCE from the remnants of the earlier Middle Assyrian Kingdom (Fig. 1, A and B, and fig. S1) (1–4). Over the course of the next two centuries, the Neo-Assyrian (hereafter, Assyrian) Empire, accompanied by an ideology of universal conquest, expanded rapidly through military campaigns and forced taxation to become the “superpower” of the Near East (3). At its height (c. early seventh century BCE), the Assyrian state stretched from Central Anatolia in the north to the Mediterranean and Egypt in the west, and eastward to the Persian Gulf and western Iran (fig. S1) (1–4). Assyrian imperial policies of forcibly deporting and integrating local populations from conquered lands to their imperial and provincial capitals (5, 6) created Assyrian capital cities with populations far greater than any third or second millennium BCE cities (7, 8). To sustain these expansive urban and rural populations, the Assyrians engineered massive road and irrigation networks (fig. S2) (8–12), enabling settlement expansion into large parts of the “dry-farming belt” including marginal and previously unsettled zones (12, 13). However, the empire plummeted from its zenith (c. 670 BCE) to complete political collapse (c. 609 BCE) in just 60 years (1–5).

Earlier explanations for the speed and totality of the Assyrian collapse have focused on the roles of imperial overexpansion, internal politico-economic conflicts, civil wars, and, in particular, Assyrian military defeat at the hands of the combined armies of Babylonians

and Medes (1–4, 14, 15). What role climate change played in shaping the course of the Assyrian Empire (16), however, has been largely ignored despite the fact that the Assyrian heartland and its hinterlands comprised a region of high interannual precipitation variability and drought vulnerability (17–20). Up to now, a lack of paleoclimate records from the region, with age control and temporal resolution comparable in precision to Assyrian historical and archaeological records, has precluded assessment of whether regional climate change contributed to the rise and/or collapse of the Assyrian Empire. Here, we present high-resolution and absolute-dated precipitation and effective moisture records over the past 4000 years from Kuna Ba Cave in northern Iraq, located ~300 km southeast of the ancient city of Nineveh (Fig. 1A and fig. S1). These data provide a climatic context for the rise, expansion, and ultimately the collapse of the Assyrian Empire during the mid-to-late seventh century BCE. Our data also permit us to place the recent multiyear droughts and a near-century-long drying trend over the eastern Mediterranean and Middle East (EMME) region (Fig. 1) (17–19), in the broader context of the region's hydroclimate variability during the past four millennia.

## Regional setting

The core of the Assyrian Empire encompassed a triangular region in northern Iraq defined by the capital cities of Assur in the south (modern Qal'at Sherqat), the seventh century BCE Assyrian capital of Nineveh (modern Mosul) in the north, and Arbela (modern Erbil) in the east (Fig. 1, A and B, and fig. S1) (3, 4). Mediterranean cyclonic systems in this region provide the bulk of annual precipitation (~90 to 95%) during the cool season (November to April), ranging from 600 to 1000 mm in the north and west to ~200 to 300 mm or less in the south and east (fig. S3A) (17–19). Today, much of the region that constituted Assyria's heartland and its hinterland is situated within the high-yield rain-fed cereal agriculture zone lying above the 200- to 300-mm isohyets, referred to as a “zone of uncertainty” (13) because interannual variability is typically 40 to 60% (Fig. 1B and fig. S3B) and rain-fed cereal cultivation is risky and unsustainable (13). During years of anomalously high and low rainfall, this agriculturally marginal zone shifts southward and northward by several hundred kilometers, rendering nearly all ancient Assyria's heartland both favorable for

<sup>1</sup>Department of Earth Science, California State University, Dominguez Hills, Carson, CA, USA. <sup>2</sup>Institute of Global Environmental Change, Xi'an Jiaotong University, Xi'an, China. <sup>3</sup>School of Forestry and Environmental Studies, Yale University, New Haven, CT, USA. <sup>4</sup>Department of Near Eastern Languages and Civilizations, Yale University, New Haven, CT, USA. <sup>5</sup>Department of Earth Sciences, University of Minnesota, Minneapolis, MN, USA. <sup>6</sup>Mitre Corporation, McLean, VA, USA. <sup>7</sup>Cooperative Institute for Research in Environmental Sciences, University of Colorado Boulder, Boulder, CO, USA. <sup>8</sup>Department of Earth and Environmental Sciences, University of Illinois, Chicago, IL, USA. <sup>9</sup>Department of History, Social Sciences University of Ankara, Ankara, Turkey. <sup>10</sup>Department of Earth Sciences, University of Southern California, Los Angeles, CA, USA.

\*Corresponding author. Email: asinha@csudh.edu (A.S.); kathayat@xjtu.edu.cn (G.K.)

†These authors contributed equally to this work.

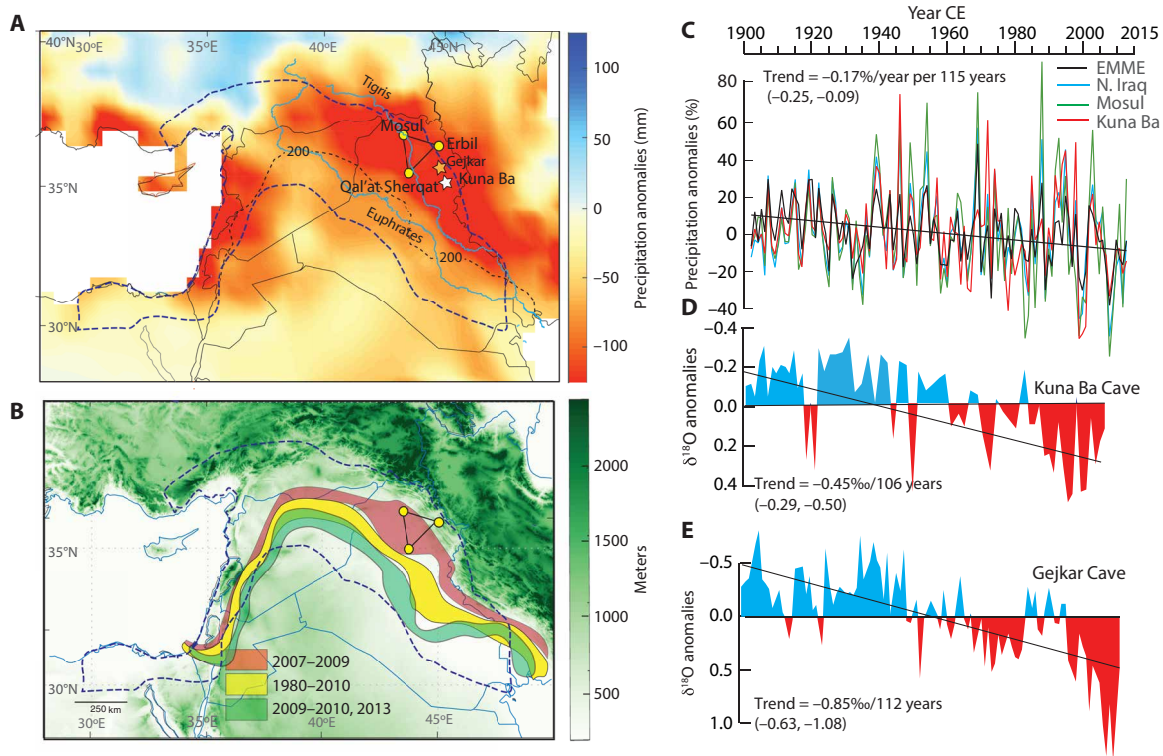


**Fig. 1. Locations, climate, proxy data, and historical context.** (A) Observed November to April (N-A) precipitation anomalies (relative to 1901–1980) during one of the most severe episodes of multiyear (2006/7–2008/09) droughts (18, 19) in the eastern Mediterranean and Middle East (EMME) ( $\sim 30^{\circ}$  to  $40^{\circ}$ N and  $30^{\circ}$  to  $50^{\circ}$ E). Gridded ( $0.5^{\circ} \times 0.5^{\circ}$ ) precipitation data are from the Global Precipitation Climatology Center (GPCC v.7) (Materials and Methods) (52). The inferred spatial extent of the Assyrian Empire at its peak ( $\sim 670$  BCE) (dashed line), traditional Assyrian heartland (triangle) (1–3), and the locations of modern cities of Mosul and Erbil (yellow circles) are shown along with the location of Kuna Ba Cave (star). (B) Shaded regions show the area bounded between the 200- and 300-mm isohyets for the dry (2007–2009), wet (2009–10, 2013), and mean climatology (1980–2010) periods. Topography data are from Global 1-min elevation collection (<https://www.ngdc.noaa.gov/mgg/global/>) (C to E) Time series of November to April GPCC precipitation anomalies (% departure from the 1901–1980 period) over the EMME and northern Iraq ( $\sim 33^{\circ}$  to  $38^{\circ}$ N and  $41^{\circ}$  to  $46^{\circ}$ E) and from the grid points closest to Mosul ( $\sim 36.5^{\circ}$ N and  $43.1^{\circ}$ E) and Kuna Ba Cave ( $\sim 35^{\circ}$ N and  $45^{\circ}$ E). (C) Kuna Ba (this study) and Gejkar cave  $\delta^{18}\text{O}$  data (21) for the 1900–2006 (D) and 1900–2012 (E) periods, respectively, as anomalies (relative to the 1900–2000 period) (shaded). Linear trends (least-squares fits of EMME and speleothem time series) that are significantly different from zero at 95% confidence level are shown with black lines.

high-yield cereal cultivation and vulnerable to crop failures (Fig. 1B). The latter was demonstrated during the severe drought episodes of 1999–2001 and 2007–2008 when cereal crop failures and widespread livestock death were pervasive across northern Syria and Iraq (18–20). These droughts, which were the most severe in the past 50 years, were marked by up to 60% reduction in cool-season rainfall over northern Iraq (Fig. 1, A and B) that exacerbated regional socio-economic conditions already suffering from decades of political instability and unsustainable socioeconomic policies (20).

## RESULTS

### Paleoclimate record

The EMME is among the most water-stressed regions in the world today. Understanding the processes that govern its complex spatio-temporal hydroclimate variability requires paleoclimate proxy reconstructions with high temporal resolution comparable to instrumental records. This is particularly crucial for regions such as northern Iraq, where decades of war and unrest have resulted in substantial gaps in instrumental observations. However, these records from the region are rare (21). We reconstructed the hydroclimate history of the region spanning the past  $\sim 4000$  years [ $\sim 57$  to 3988 years

before the present (yr B.P.), where B.P. = 1950 AD] by using the stable oxygen ( $\delta^{18}\text{O}$ ) and carbon ( $\delta^{13}\text{C}$ ) isotope measurements ( $N = 1725$ ) from two speleothems (NIR-1 and NIR-2) (table S1), which were collected from Kuna Ba Cave [ $35^{\circ}09'32''\text{N}$  and  $45^{\circ}38'47''\text{E}$ ;  $\sim 660$  m above sea level (masl)] located near the city of Sulaymaniyah in the Kurdistan region of northeastern Iraq, approximately 300 km southeast of Nineveh (Fig. 1, A and B, and figs. S1 and S3A). The chronologies of NIR-1 and NIR-2 are constrained by 11 and 19  $^{230}\text{Th}$  dates, respectively (Fig. 2, fig. S4, and table S2). Applications of different age-modeling schemes (Materials and Methods) yielded nearly identical age models (fig. S4). Excellent replications between the NIR-1 and NIR-2  $\delta^{18}\text{O}$  and  $\delta^{13}\text{C}$  profiles on their independent age models (Fig. 2) strongly suggest that the records contain the regional climate signal and that the speleothem calcite precipitated at or near isotopic equilibrium conditions (Materials and Methods and fig. S5). The composite (NIR)  $\delta^{18}\text{O}$  and  $\delta^{13}\text{C}$  profiles provide an average temporal resolution of  $\sim 3$  years with an average temporal uncertainty of  $\sim 25$  years ( $1\sigma$ ) over most portions of our record (Materials and Methods).

Cave monitoring data and our  $\delta^{18}\text{O}$  measurements of drip water and cool-season precipitation near the cave further indicate that (i) the speleothem calcite precipitation in Kuna Ba Cave occurs at or near isotopic equilibrium condition, (ii) the cave's karstic system

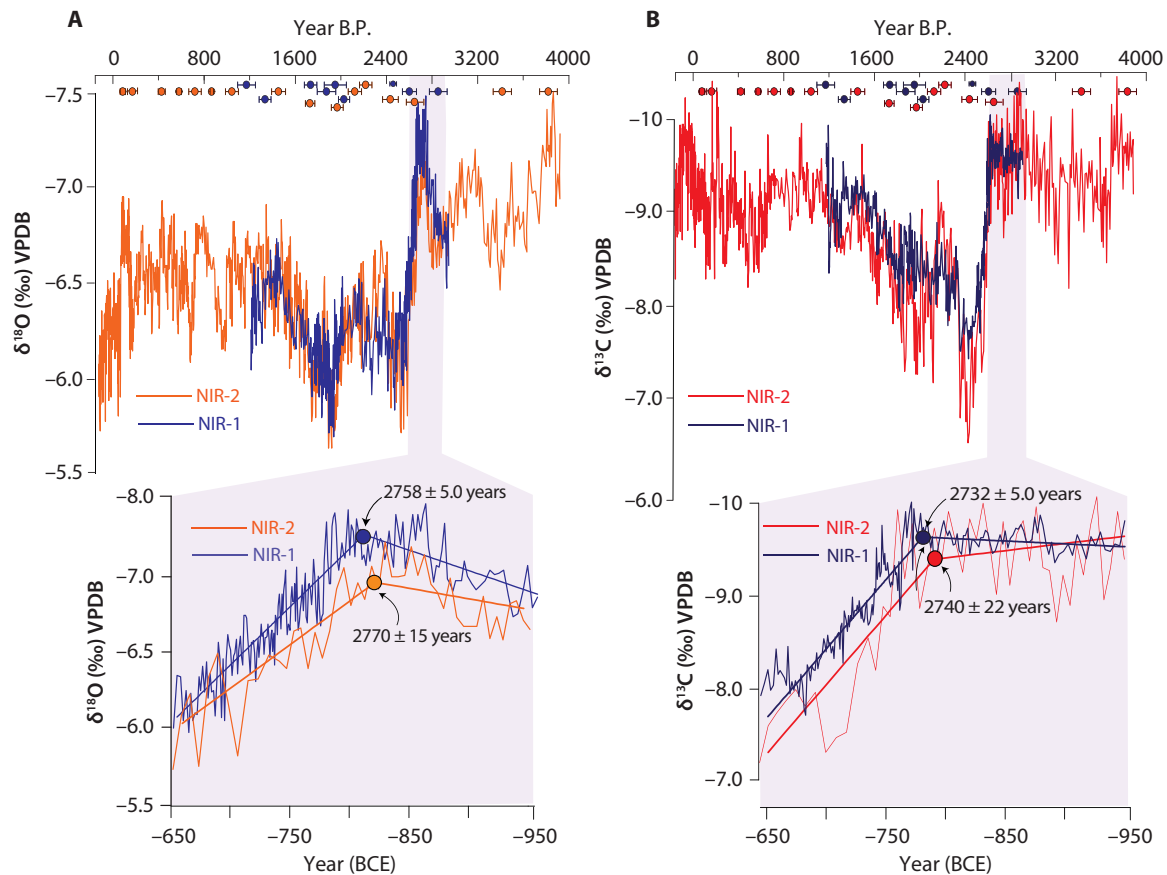


**Fig. 2. Kuna Ba Cave  $\delta^{18}\text{O}$  and  $\delta^{13}\text{C}$  profiles and change point estimation.** (A)  $\delta^{18}\text{O}$  profiles of NIR-1 (dark blue) and NIR-2 (orange) and  $^{230}\text{Th}$  dates with  $2\sigma$  error (color-coded by speleothems). (B)  $\delta^{13}\text{C}$  profiles of NIR-1 (blue) and NIR-2 (red) and  $^{230}\text{Th}$  dates with  $2\sigma$  error (color-coded by speleothems). The insets in both panels show the timings of initial changes in the  $\delta^{18}\text{O}$  and  $\delta^{13}\text{C}$  profiles between 2600 and 2900 B.P. using an objective approach (Materials and Methods) (49). Change points and associated  $1\sigma$  errors (relative to the age model chronology) are marked by solid circles (color-coded) and numbers.

is recharged by cool-season rainfall, (iii) and the  $\delta^{18}\text{O}$  of speleothem reflects seasonally averaged  $\delta^{18}\text{O}$  of precipitation ( $\delta^{18}\text{O}_p$ ) (fig. S5). Several lines of empirical, modeling, and proxy observations suggest that temporal variations in the Kuna Ba  $\delta^{18}\text{O}$  and  $\delta^{13}\text{C}$  records provide changes in the regional precipitation amount and the local precipitation-evaporation balance (Supplementary Text). These include (i) coherent positive trends in the speleothem  $\delta^{18}\text{O}$  profiles of Kuna Ba and the nearby Gejkar cave (Fig. 1, D and E) (21), mirroring a century-scale drying trend ( $\sim 15$  to 20% decline in the cool-season precipitation since the 1930s) over the EMM region (Fig. 1C and fig. S6) (17–19) [a relatively muted Kuna Ba speleothem  $\delta^{18}\text{O}$  profile compared to instrument data highlights how speleothems typically smooth the climate signal in regions marked by high inter-annual variability (Fig. 1D); sustained periods of higher (and asymmetric) occurrences of drier (wetter) seasons, however, can skew the speleothem  $\delta^{18}\text{O}$  toward more enriched (depleted) values]; (ii) a positive covariance between the Kuna Ba  $\delta^{18}\text{O}$  and  $\delta^{13}\text{C}$  profiles (Fig. 2) ( $r = 0.48$ ,  $P = 0.018$ ), which is typical of speleothem records from arid regions, because drier conditions result in slower infiltration rates and increased degassing, which drive higher  $\delta^{18}\text{O}$  and  $\delta^{13}\text{C}$  values and vice versa (21, 22); and (iii) the presence of a prominent inverse relationship between the oxygen isotope composition of precipitation ( $\delta^{18}\text{O}_p$ ) and precipitation amount in EMM (23–25),

consistent with the simulated data from the isotope-enabled general circulation model ECHAM5-wiso (fig. S7) (26).

## DISCUSSION

### Assyrian megapluvial and megadrought

The Kuna Ba  $\delta^{18}\text{O}$  and  $\delta^{13}\text{C}$  records display a range of  $\sim 2.0$  and  $2.5\%$ , respectively, revealing a wide spectrum of hydroclimate variability consisting of multicentennial trends and quasi-oscillatory variability together with step-like shifts in the mean climate of the region over the past 4000 years (fig. S8A). Distinct multidecadal to centennial length intervals of “drier” and “wetter” conditions are defined by substantially enriched and depleted  $\delta^{18}\text{O}$  values (see Materials and Methods) (Fig. 3 and fig. S8B). To highlight multidecadal- to centennial-scale variability, we removed the long-term ( $>500$  years) nonlinear trends from the composite  $\delta^{18}\text{O}$  record (Materials and Methods). The  $z$  score transformed values of the detrended record delineating the drier intervals are similar to the values observed during the  $\sim 1980$ –2007 period of our record (Fig. 3 and fig. S8), the latter coeval with the period of the largest reduction in cool-season precipitation over the northern Iraq and Syria during the past century (18, 19). The interval between  $\sim 2800$  and  $2690$  yr B.P. ( $\sim 850$  and  $740$  BCE) emerged as one of the wettest periods of the past 4000 years

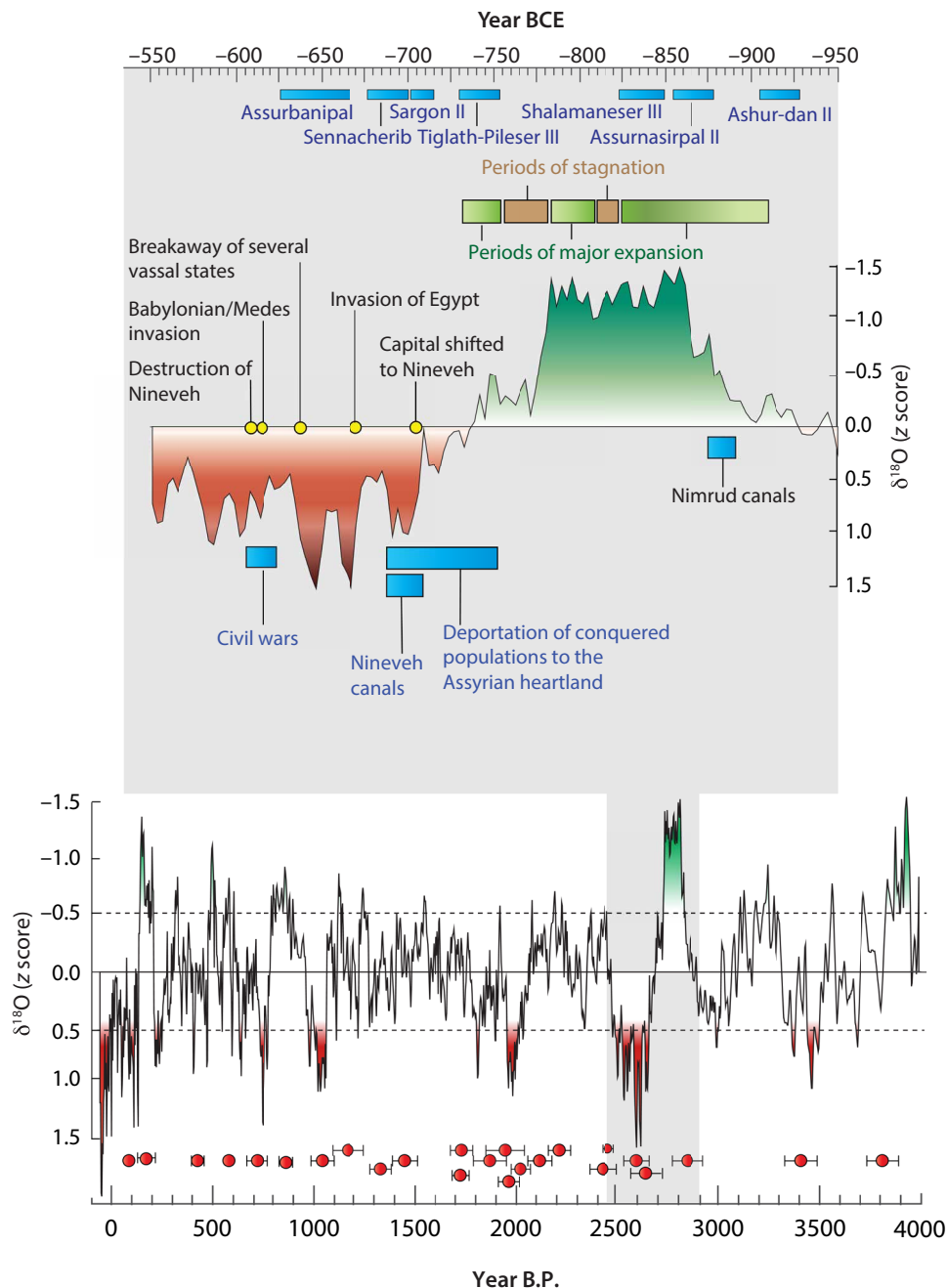


**Fig. 3. Comparisons between the detrended Kuna Ba cave z score transformed  $\delta^{18}\text{O}$  record and the key Assyrian historical events.** The detrended and normalized  $\delta^{18}\text{O}$  record (this study) delineates a number of subdecadal to multidecadal periods of inferred drought (z score > 0.5, brown) and pluvial conditions (z score < -0.5, green). The inset shows the  $\delta^{18}\text{O}$  record between 550 and 950 BCE (shaded, with increasing saturation index representing increasing intensity) and the major historical Assyrian events delineated by horizontal color bars, yellow dots, and supporting text. Approximate reigns of the key Assyrian kings are shown with horizontal bars (cyan). Red circles and error bars mark  $^{230}\text{Th}$  dates with  $2\sigma$  error. The chronology of Neo-Assyrian rulers and imperial events is primarily based on the dating of the Būr-saggiġe eponym to the solar eclipse of 15 June 763 BCE (see also the Supplementary Materials for more information) (27). The age errors associated with historical events are known with annual and, for many events such as the Fall of Nineveh in 612 BCE, at monthly chronological precision (27).

in the Kuna Ba record, representing ~15 to 30% increase in the cool-season precipitation amount (relative to 1980–2007 CE) as inferred from the observed modern speleothem  $\delta^{18}\text{O}$ -precipitation relationship (Figs. 1, C to E, and 3). This peak wet period, termed here the Assyrian megapluvial, was embedded within nearly two centuries (~925–725 BCE) of pluvial conditions and is synchronous with the

prominent phases of the Assyrian imperial expansion (c. 920–730 BCE) (1–4) within the margin of dating errors of both proxy (~25 years,  $1\sigma$ ) and historical records (~1 year) (Fig. 3). The age errors associated with the events surrounding the rise and fall of the Assyrian Empire are known with annual and, for many events, at monthly chronological precision (Supplementary Text) (27).

The near-simultaneous increases in the Kuna Ba  $\delta^{18}\text{O}$  and  $\delta^{13}\text{C}$  values between  $\sim 2750$  yr B.P. ( $\sim 800$  BCE) and  $\sim 2650$  yr B.P. ( $\sim 700$  BCE) (Figs. 2 and 3) mark the transition from peak pluvial to peak dry conditions. The timings of initial “change points” in all four isotopic profiles (Fig. 2 and Materials and Methods) indicate that the  $\delta^{13}\text{C}$  values lagged changes in the  $\delta^{18}\text{O}$  values by  $\sim 30$  to 50 years, consistent with an expected slower response of speleothem  $\delta^{13}\text{C}$  due to longer turnover time of organic carbon in response to changes in local effective moisture and/or precipitation. The interval between  $\sim 2650$  and  $2500$  yr B.P. ( $\sim 675$ – $550$  BCE) in the detrended record delineated by some of the highest  $\delta^{13}\text{C}$  values and  $\delta^{18}\text{O}$  values emerged as a  $\sim 125$ -year period of peak aridity, termed here the Assyrian megadrought, which is synchronous, within the margins of dating error, with the period of the Assyrian imperial collapse (c. 660–600 BCE) (Fig. 3) (1–4). The severity of the Assyrian megadrought is comparable in magnitude to the post-1980 CE drought inferred from our speleo-

them record—an observation that provides critical context for both historical and modern droughts (17, 18).

Imprecise chronologic constraints and/or substantially coarser temporal resolutions of most of the existing proxy records from the EMME region preclude a definitive assessment of the spatial and temporal signatures of the Assyrian megadrought and megapluvial events (Fig. 4). Nonetheless, the transition from the megapluvial to the megadrought conditions in our record between  $\sim 2.6$  and  $2.7$  ka B.P. matches in timing with a hemispheric scale and possibly a global-scale climate event, generally referred in the literature as the 2.7- or 2.8-ka event [see review in (28)]. The shift from wetter to drier conditions at  $\sim 2.7$  ka B.P. is also evident in a high-resolution speleothem  $\delta^{18}\text{O}$  record from Jeita cave in the northern Levant (22) as well as in some lake, marine, and speleothem proxy records from the eastern Mediterranean, Turkey, and the Middle East (Fig. 4) [e.g., (29–37)], although the exact timing of this transition varies between records

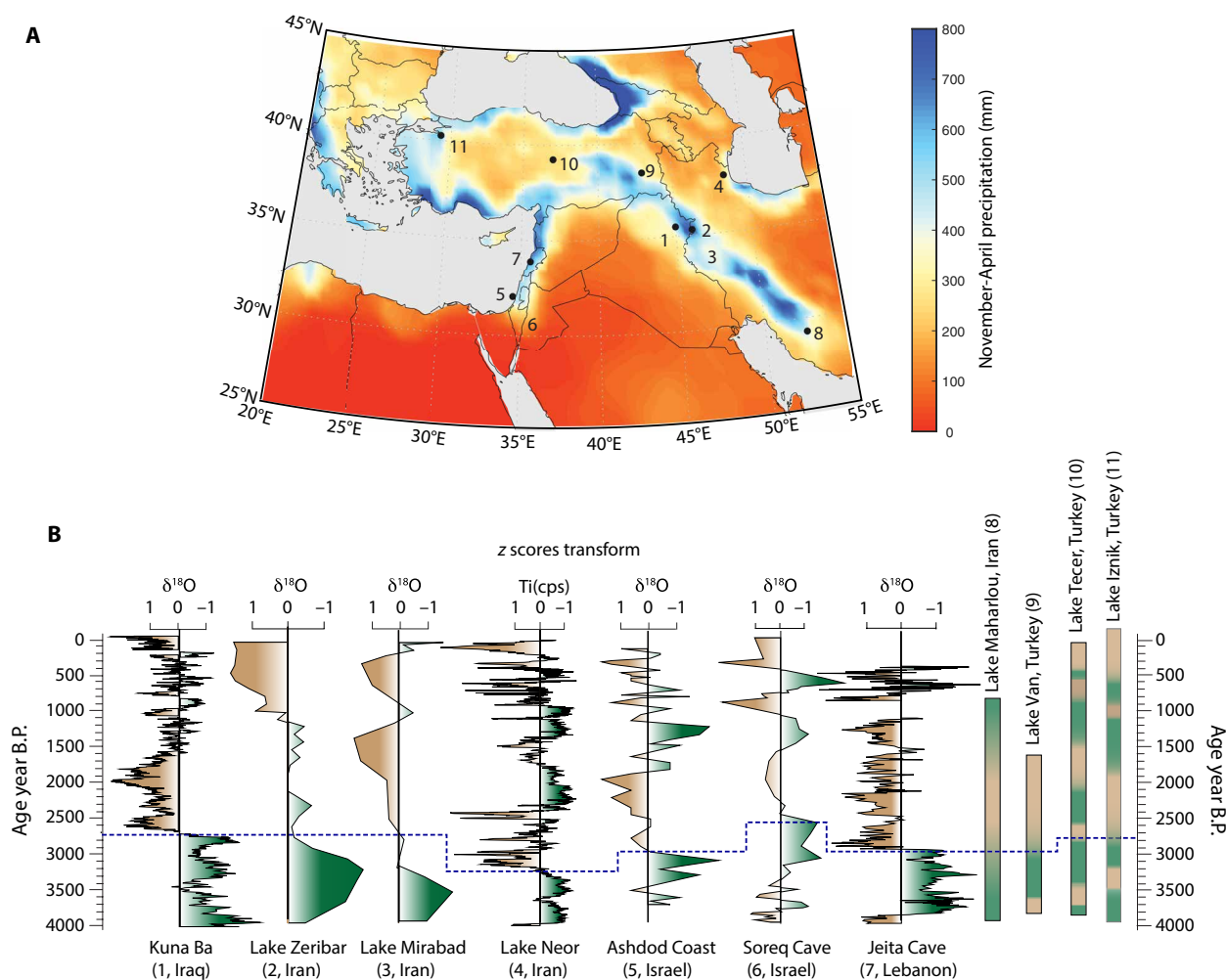


**Fig. 4. Comparison between Kuna Ba and regional proxy records.** (A) Spatial map showing the November to April precipitation amount (GPCP) and locations of the proxy records (black circles and numbers). (B) Collection of z score transformed regional proxy climate records showing wetter (green) and drier (brown) conditions over the past 4000 years. Names and locations of the proxy records are noted, and the numbers correspond to the proxy locations on the map. Proxy records from left are as follows: (1)  $\delta^{18}\text{O}$  of Kuna Ba (this study) cave speleothem; (2)  $\delta^{18}\text{O}$  of carbonate from Lake Zeribar (29) and (3) Lake Mirabad (30); (4), x-ray fluorescence–based elemental abundance of Ti in the Neor Lake sediments (31); (5)  $\delta^{18}\text{O}$  of planktonic foraminifera *Globigerinoides ruber* from the eastern Mediterranean near the Ashdod coast, Israel (32); and (6 and 7)  $\delta^{18}\text{O}$  of speleothem from Soreq (33) and Jeita caves (22). Starting from left, vertical bars show approximate temporal durations of inferred drier (brown) and wetter (green) conditions as reported by the authors of original studies from Lake Maharlou (34), Lake Van (35), Tecer Lake (36), and Lake Iznik (37). Dashed line marks a regime shift from wetter to drier conditions in most proxy records at around 2.7 ka B.P.

(Fig. 4). A comparison between the Kuna Ba and nearby Gejkar cave speleothem records show a broadly similar pattern of multidecadal variability superimposed over a statistically significant drying trend in both records over the past millennium (fig. S8C). However, the two records exhibit marked differences between the 1.6- and 2.4-ka period (fig. S8C) when the chronologic constraints in the Gejkar cave record are considerably less precise (21).

### Climate change and Assyrian agriculture

Like all ancient Mesopotamian states, the Assyrian Empire was fundamentally an agrarian society, and consequently, control of agriculturally productive land was the primary means for generating wealth (38). Because Assyrian rain-fed agriculture was highly dependent on cool-season precipitation, it is instructive to examine the relationship between precipitation variability and agriculture productivity in the geographic context of the Assyrian core area in present-day northern Iraq. Observational data show that, during years when mean annual precipitation in the region is 15 to 30% higher than the climatological mean, the zone of uncertainty lies substantially southward of the Assyrian heartland, resulting in conditions favorable for rain-fed agriculture over land that would not be arable without irrigation (Fig. 1B and fig. S9, A and B). Using “wet years” as a modern analog, we suggest that “Assyrian megapluvial” conditions would have strengthened the Assyrian agrarian economy and powered the imperial campaigns supported by the state’s agricultural revenues (38). Recent archeological surveys in the central and northern parts of the Kurdistan region of Iraq suggest that a key feature of Assyrian expansion during this period involved conquest of previously unsettled dry steppe terrain (Neo-Assyrian *madbarum*) in the capitals’ hinterlands (12). Ongoing surveys also indicate that this period was marked by execution of imperial “control technologies” to materially and ideologically commemorate the landscape through large-scale construction of hydraulic systems of regional scale, establishment of large fortified capital and provincial cities together with the forced migration of deportees, and the creation of a dense network of small rural settlements (12).

Our analysis of solar-induced chlorophyll fluorescence (SIF), a proxy for photosynthesis and a strong predictor of cereal crop yield (39) together with other satellite-based vegetation indices, shows marked changes in vegetation and crop productivity (20) during periods of drought in this region. The SIF analysis quantitatively shows that the cereal crop yield over northern Iraq is highly sensitive to rainfall changes between 200 and 400 mm but is minimally sensitive to rainfall variations above 400 mm (fig. S9D). Therefore, a northward displacement of 200 to 300 mm isohyets during the Assyrian megadrought can situate a large portion of the historical region of Assyrian heartland and hinterland under conditions where vegetation productivity would have plummeted (fig. S9A). A similar scenario playing out frequently during the first half of the seventh century BCE would have dealt a major blow to the Assyrian rain-fed agrarian economy in northern Mesopotamia (8, 10–16, 40) through frequent and widespread crop failures notwithstanding the massive irrigation networks that Assyria had put in place around Nineveh (c. 702 and 688 BCE) (fig. S2) (9–12) to sustain the estimated 4.5 million deportees that were settled mostly in the Assyrian heartland (6). Given that the Assyrian megadrought occurred in the context of widespread regional aridity and that Assyrian agricultural production probably reached maximum capacity (16), there were little means to import food from adjacent regions due to the friction of animal traction cereal transport

(7). The frequent crop failures during the Assyrian megadrought may thus have exacerbated the political unrest in Assyria in its final decades by inflaming preexisting tensions both within Assyrian society and between the Assyrians and conquered subject peoples like the Babylonians and Medes (Supplementary Text) (1–5).

### Post-Assyrian period

There is little historical or archaeological information to assess what became of the Assyrian heartland and its hinterlands’ population following the empire’s conquest and collapse in 608 BCE. In the heartland, the destruction levels of palaces, temples, and residential areas were followed by collapse strata with rare signs of paltry reconstruction and minor “squatter” occupations during the extended drought period (14, 40). At the provincial capital Sheikh Hamad/Dur-katlimmu, 200 km west of Assur, the last four Neo-Assyrian tablets are dated to only a decade after the fall of Nineveh (41). Towns and village populations of the hinterland also abandoned the region, with similar abandonments along the lower Khabur River, where ~71% of all sites disappeared rapidly (42). The populations of the desiccated heartland may have habitat-tracked to southern Mesopotamian refugia, where Neo-Babylonian irrigation-based agriculture remained less vulnerable to megadrought and soon expanded greatly to feed hypertrophic cities. This absence of sedentary north Mesopotamian agricultural settlement noticed by Xenophon (Anab. III, 4) in 401 BCE, and with only rare exceptions at riverine refugia such as Nisibina, persisted past the return of pre-megadrought precipitation until the Seleucid and Parthian settlement revivals that began in the late fourth century BCE (43).

### CONCLUSIONS

The fall of the Assyrian Empire was one of the iconic events of world history. The chain of events leading to its rise, expansion, and downfall likely included multiple proximal and distal factors. The past few decades of the empire were marked by political instability, civil wars, and, ultimately, invasion by the combined armies of Babylonians and Medes (1–4), which were perhaps among the proximate causes for the Assyrian collapse. Our data suggest that climate change was an underlying causal factor, whose effects on the Assyrian imperial economy began centuries before the Empire’s collapse. Nearly two centuries of high precipitation and high agrarian outputs encouraged high-density urbanization and imperial expansion that was not sustainable when climate shifted to megadrought conditions during the seventh century BCE. Megadroughts as severe as modern droughts in the region but lasting for multiple decades likely crippled the Assyrian economy and precipitated its collapse. Our data also suggest that the recent multiyear droughts superimposed over a century-long drying trend are among the worst episodes of drought in the region’s hydroclimate variability during the past four millennia.

### MATERIALS AND METHODS

#### Field collection and sample preparation

Kuna Ba Cave (~500 m in length; ~660 masl; 35°09′32″ N and 45°38′47″ E) is located near the city of Sulaymaniyah (Supplementary Text). Two speleothems (stalagmites)—NIR-1 (~121 mm) and NIR-2 (~406 mm)—were collected ~150 and 300 m from the cave’s entrance, respectively. NIR-2 was actively growing at the time of collection (November 2007). Fresh calcite growth was induced on a frosted glass

plate beneath the feeder drip of NIR-2 after its removal. The cave's ambient temperature and the relative humidity (RH) at the time of sample collection were  $\sim 18.0^\circ\text{C}$  and 95%, respectively. Drip water samples were subsequently collected in August 2008, November 2011, and February and June 2012. The average  $\delta^{18}\text{O}$  of drip water, RH, and temperature are  $-6.17 \pm 0.5\text{‰}$  ( $n = 21$ ),  $95 \pm 2\%$ , and  $18^\circ \pm 1.0^\circ\text{C}$ , respectively (fig. S5).  $\delta^{18}\text{O}$  of modern calcite scraped from the center of the glass plate is  $-6.24 \pm 0.08\text{‰}$ , consistent with the theoretical  $\delta^{18}\text{O}$  values of calcite precipitated at the equilibrium isotopic condition (fig. S5). A program of daily rainfall collection was conducted between January and March 2012 at the University of Sulaimani, Sulaymaniyah, located  $\sim 30$  km from the Kuna Ba cave.  $\delta^{18}\text{O}_p$  of precipitation over this period ranged from  $\sim -2.40$  to  $-10.45\text{‰}$ , with an amount-weighted average value of  $-6.05\text{‰}$  ( $n = 20$ ), similar to the average  $\delta^{18}\text{O}$  value of the drip water samples ( $-6.17\text{‰}$ ,  $n = 24$ ). The stalagmites were cut with a thin diamond blade along the growth axes and lightly polished. An automated triaxial micromill was used to obtain subsamples for stable isotopic analyses by continuously milling in 100- $\mu\text{m}$  increments along the growth axis of NIR-1 (between  $\sim 18$  and 121 mm from the top) and NIR-2 (between 0 and  $\sim 401$  mm, with 0 being top of the sample) (table S1). Subsamples for  $^{230}\text{Th}$  dating (weighing typically between 150 and 300  $\mu\text{g}$ ) were obtained by drilling with a 0.9-mm carbide dental burr.

### Stable isotope measurement

The NIR-1 and NIR-2 profiles consist of 625 and 1100 stable isotope measurements (table S1). Subsamples for  $\delta^{18}\text{O}$  and  $\delta^{13}\text{C}$  analyses were measured using a Multi-Prep dual inlet system attached to an isoprime stable isotope ratio mass spectrometer at the University of Southern California. The long-term precision of the Ultissima standard for the  $\delta^{18}\text{O}$  and  $\delta^{13}\text{C}$  measurements over the course of this study was  $\sim 0.06$  and  $0.03\text{‰}$ , respectively.

### $^{230}\text{Th}$ dating

The chronological frameworks of NIR-1 and NIR-2 records were established by 11 and 19  $^{230}\text{Th}$  dates, respectively (table S2).  $^{230}\text{Th}$  dating was performed at the University of Minnesota and at Xi'an Jiaotong University, China, by using Thermo-Finnigan Neptune/Neptune plus multi-collector inductively coupled plasma mass spectrometers. The methods are identical in both laboratories. We used standard chemistry procedures (44) to separate uranium and thorium. A triple-spike ( $^{229}\text{Th}$ - $^{233}\text{U}$ - $^{236}\text{U}$ ) isotope dilution method was used to correct instrumental fractionation and to determine U/Th isotopic ratios and concentrations (45). U and Th isotopes were measured on a MasCom multiplier behind the retarding potential quadrupole in the peak-jumping mode using standard procedures (45). Uncertainties in U/Th isotopic measurements were calculated offline at the  $2\sigma$  level, including corrections for blanks, multiplier dark noise, abundance sensitivity, and contents of the same nuclides in spike solution. Corrected  $^{230}\text{Th}$  ages assume an initial  $^{230}\text{Th}/^{232}\text{Th}$  atomic ratio of  $4.4 \pm 2.2 \times 10^{-6}$ , the values for a material at secular equilibrium with a bulk earth  $^{232}\text{Th}/^{238}\text{U}$  value of 3.8 (45).

### Statistical analyses

#### Age models

The NIR-1 and NIR-2 age models and associated age uncertainties were modeled using COPRA (Constructing Proxy Records from Age model) (46), Bchron (47), and OxCal (48) age-modeling schemes (fig. S4). All three modeling schemes yielded nearly identical age

models, and the conclusions of this study are not sensitive to the choice of any one age model. We adopted COPRA age models and generated 2000 realizations to account for the dating uncertainties (2.5 and 97.5% quantile confidence limits). The temporal resolution of NIR-2 on COPRA age models ranges from 0.5 to 12 years, with an average resolution of  $\sim 4$  years. The average temporal resolution of NIR-1 is  $\sim 2.8$  years. The NIR-1 and NIR-2 isotope profiles during the period of overlap were averaged to derive a composite record (average temporal resolution of  $\sim 3$  years).

#### Change point estimation

We applied a parametric nonlinear regression technique (49) to constrain the timings of initial changes in Kuna Ba isotope profiles marking the transition from the Assyrian megapluvial to Assyrian megadrought state (Fig. 2). This method uses a continuous function consisting of two linear parts that are joined at the break point. The break model was fitted to data using a weighted least-squares method with a brute-force search for the break point. Statistical uncertainties of the trend, timing, and break point were evaluated using 2000 bootstrap simulations, which preserved the distribution and serial dependence of the data over the length of a block (49). Change point estimations in the  $\delta^{18}\text{O}$  profiles predated changes points in the  $\delta^{13}\text{C}$  profiles by  $\sim 30$  to 50 years (Fig. 2).

#### Detrending

We used singular spectrum analysis (SSA) (50) to remove nonlinear trends ( $>500$  years) from the composite NIR  $\delta^{18}\text{O}$  time series. The SSA method decomposes time series into several modes of variability (monotonic and oscillatory) and the remaining low-amplitude high-frequency noise. Before applying SSA, the time series was linearly interpolated (2.98-year interval) to match the number of data points in the original composite time series. The time series was detrended by removing the first component (i.e., largest eigenvalue from an auto covariance matrix of SSA). The size of the embedded window was set to one-fifth the size of the length of the time series. The detrended time series was normalized by its mean and SD to produce  $z$  scores.

#### Precipitation data analysis

Assessments of precipitation trends and anomalies in both spatial and temporal domain evolution can be sensitive to the choice of gridded precipitation data. This is particularly important for regions such as northern Iraq, where the sparseness of station gauge data before the 1930s and after the 1980s precludes a definitive assessment of centennial-scale trend at the local scale. A recent study (51) applied the compromise programming approach to evaluate several widely used gridded datasets and concluded that gauge-based high-resolution ( $0.5^\circ \times 0.5^\circ$ ) Global Precipitation Climatology Centre (GPCC) version 7 (52) global datasets of observed monthly precipitation best replicate annual and seasonal mean and variability and probability distribution of observed precipitation from 41 stations located within and surrounding Iraq. Consequently, we used the GPCC product to extract November to April precipitation data over the EMME ( $\sim 30^\circ$  to  $40^\circ\text{N}$  and  $30^\circ$  to  $50^\circ\text{E}$ ) and northern Iraq ( $\sim 33^\circ$  to  $38^\circ\text{N}$  and  $41^\circ$  to  $46^\circ\text{E}$ ) and from the grid points closest to Mosul ( $36.35^\circ\text{N}$  and  $43.16^\circ\text{E}$ ) and Kuna Ba Cave ( $35.09^\circ\text{N}$  and  $45^\circ\text{E}$ ) (Fig. 1B). These data were used to analyze the spatial precipitation trends (fig. S6, A and B), anomalies (Fig. 1, A and C), amounts (figs. S3, S6, D and F, and S9), and the mean positions of the isohyets for different time periods as discussed in the text (Fig. 1B and fig. S9, A and B). We also used the University of East Anglia Climatic Research Unit (CRU) version 4.1 (53) to estimate precipitation trends during the instrumental period (fig. S6A). The GPCC and CRU datasets are in close agreement,

but some differences exist before the 1930s because of the sparseness of observational data before the 1930s. Station data from Mosul and Sulaymaniyah (available with gaps between 1923 and 1980 and 1941 to 2004, respectively) were also used (fig. S3C). The precipitation amount and isohyets for wet and dry composites (fig. S9, A and B) were constructed by using the GPCC data. The composites represent means of November to April precipitation amount for the 10 driest (2012, 2008, 2007, 2000, 1999, 1986, 1984, 1983, 1958, and 1935) and 10 wettest (1987, 1985, 1980, 1976, 1961, 1941, 1936, 1923, 1920, and 1903) years, which were identified from the GPCC data.

### Trend analysis

Statistical significance of linear trends in precipitation and speleothems  $\delta^{18}\text{O}$  time series from Kuna Ba and Gejkar caves (Fig. 1C and fig. S6A) was evaluated by generating 95% bootstrapped confidence intervals ( $N = 2000$ ). Trends significance for gridded precipitation data at each grid point at 95% confidence level (fig. S6B) was determined by using a nonparametric modified Mann-Kendall's test that accounts for serial autocorrelation in data.

### Solar-induced chlorophyll fluorescence

We used monthly gridded SIF from the Global Ozone Monitoring Experiment-2 (GOME-2) MetOp-A satellite, which measures the spectrum for top-of-atmosphere radiance between 240 and 790 nm. Data between 734 and 758 nm were used to estimate the SIF following the methods described by Joiner *et al.* (54). The level 3 GOME-2 SIF product was prescreened for clouds ( $\geq 30\%$  cloud coverage was excluded) and has undergone limited validation with ground data and other satellite products (54). We used data from the period 2007 to 2017 from the most current version available at the time of the study (version 27). The footprint of the retrieval was 40 km by 80 km before July 2013 and 40 km by 40 km afterward. The data were archived onto a  $0.5^\circ$  grid. We extracted the mean November for April SIF for each grid cell shown with a unit of  $\text{mW m}^{-2} \text{nm}^{-1} \text{sr}^{-1}$ . SIF measurements were binned into 50-mm precipitation windows to assess the average SIF associated with different amounts of cool-season precipitation. Average SIF retrievals from 2007 to 2017 for each grid cell were co-located with precipitation and then binned into 50-mm precipitation bins. To estimate sensitivity, we calculated the rate of change of SIF for each incremental change in precipitation.

### Isotopic equilibrium tests

Conventional criteria to assess the isotopic equilibrium of stalagmites require no correlation between  $\delta^{18}\text{O}$  and  $\delta^{13}\text{C}$  along the same growth laminae (55). The latter has proven to be difficult, and in some cases, it has been demonstrated that a lack of correlation between  $\delta^{18}\text{O}$  and  $\delta^{13}\text{C}$  values along the speleothem's flanks does not preclude deposition of calcite in isotopic conditions at or near the growth axis (56). Instead, the replication test (i.e., a high degree of coherence between  $\delta^{18}\text{O}$  profiles of individual speleothems from the same or nearby cave) is a more rigorous and reliable test of isotopic equilibrium (56). A high degree of visual similarity between the coeval portions of NIR-1 and NIR-2  $\delta^{18}\text{O}$  profiles suggests that both stalagmites record primary climate signals. The visual comparison was further confirmed by statistically significant correlations between the NIR-1 and NIR-2  $\delta^{18}\text{O}$  profiles ( $r = 0.66$ , which is significant at 95% confidence level) using ISCAM algorithm (57). The significance levels were assessed against a red-noise background generated by using artificially simulated first-order autoregressive time series (AR1). Furthermore, a strong replication between the NIR-1 and NIR 2  $\delta^{13}\text{C}$  profiles ( $r = 0.81$ ) is suggestive of isotopic equilibrium precipitation of calcite. Last, the coherence between the measured  $\delta^{18}\text{O}$  values of

calcite obtained from the tip of actively growing NIR-2 and glass plates under feeder drips with the theoretical range in  $\delta^{18}\text{O}$  values of calcite precipitated in isotopic equilibrium condition (fig. S5) supports the idea that calcite deposition in Kuna Ba cave occurs at or close to isotopic equilibrium conditions.

### ECHAM5-wiso simulated data

We used an isotope-enabled general circulation climate model ECHAM5-wiso (26) data to understand the dynamic controls of  $\delta^{18}\text{O}_p$  variability over the EMME. We used data from a historical climate simulation (1871 to 2011) with this model at T106 ( $1^\circ$  resolution) (58) for this study. The ECHAM5-wiso has been widely used for both modern and past climate and isotope simulations and has been shown to be in good agreement with available  $\delta^{18}\text{O}_p$  observations from the Global Network of Isotopes in Precipitation (GNIP) on an annual and seasonal time scale (26). We further validated the model using two of the longest GNIP  $\delta^{18}\text{O}$  datasets from the region, namely, Adana, Turkey (monthly  $\delta^{18}\text{O}_p$  data available from 1980 to 2011), and Tehran, Iran (monthly  $\delta^{18}\text{O}_p$  data available from 1960 to 1980) (fig. S7, C and E). Spatial pattern of simulated precipitation amount from ECHAM5-wiso correctly captures the observed spatial pattern of the cool-season (November to April) precipitation amounts and  $\delta^{18}\text{O}_p$  over the EMME. The model's finer resolution provides a realistic representation of strong east-west and north-south gradient in both precipitation amount and  $\delta^{18}\text{O}_p$  over the broader EMME region (fig. S7, A, B, and G) as well as across Iraq and Syria, which agree reasonably well with the observed data (59, 60). The model results show moderate to strong inverse correlation between the amount-weighted  $\delta^{18}\text{O}_p$  extracted from the grid point closest to Kuna Ba with upstream regional precipitation amount, consistent with results of previous empirical studies from the region [e.g., (23–25)].

### SUPPLEMENTARY MATERIALS

Supplementary material for this article is available at <http://advances.sciencemag.org/cgi/content/full/5/11/eaax6656/DC1>

Supplementary Text

Fig. S1. The geographic context of the Neo-Assyrian Empire and major Assyrian cities.

Fig. S2. The geographic context of the key Neo-Assyrian canal systems.

Fig. S3. The climatic context of the study area.

Fig. S4. Age models of NIR-1 and NIR-2 and scanned images of speleothems.

Fig. S5.  $\delta^{18}\text{O}$  of rainfall, drip water, and modern calcite.

Fig. S6. Regional precipitation trends and anomalies.

Fig. S7. Observed and simulated precipitation amount and  $\delta^{18}\text{O}_p$ .

Fig. S8. Comparison between Kuna Ba and regional proxy records.

Fig. S9. Spatial maps of precipitation composites and SIF.

Table S1. Stable isotope data.

Table S2. U-series data.

References (61–79)

### REFERENCES AND NOTES

1. A. K. Grayson, *Assyrian Rulers of the Early First Millennium BC* (University of Toronto Press, 1991).
2. K. Radner, The Assur-Nineveh-Arbela Triangle: Central Assyria in the Neo-Assyrian period, in *Between the Cultures: The Central Tigris Region in Mesopotamia from the 3<sup>rd</sup> to the 1<sup>st</sup> Millennium BC*, P. Miglus, S. Mühl, Eds. (Heidelberger Orientverlag, 2011), pp. 321–329.
3. K. Radner, The Neo-Assyrian Empire, in *Imperien und Reiche in der Weltgeschichte*, M. Gehler, R. Rollinger, Eds. (Harrassowitz, 2014), pp. 101–120.
4. M. Liverani, *Assyria: The Imperial Mission* (Winona Lake, Eisenbraun's, 2017).
5. S. Parpola, The Neo-Assyrian ruling class, in *Studies on Ritual and Society in the Ancient Near East*, T. Kämmerer, Ed. (Walter de Gruyter, 2007), pp. 257–274.
6. B. Oded, *Mass Deportations and Deportees in the Neo-Assyrian Empire* (Reichert, 1979).
7. H. Weiss, The origins of Tell Leilan and the conquest of space in third millennium Mesopotamia, in *The Origins of Cities in Dry-Farming Syria and Mesopotamia in the Third Millennium BC*, H. Weiss, Ed. (Four Quarters Publishing Co., 1986), pp. 71–108.



8. T. J. Wilkinson, *Archaeological Landscapes of the Near East* (University of Arizona Press, 2003).
9. J. Ur, Sennacherib's northern Assyrian canals: New insights from satellite imagery and aerial photography. *Iraq* **67**, 317–345 (2005).
10. A. M. Bagg, Irrigation in northern Mesopotamia: Water for the Assyrian capitals (12th–7th centuries BC). *Irrig. Drain. Syst.* **14**, 301–324 (2000).
11. H. Reculeau, *Climate, Environment and Agriculture in Assyria in the 2nd Half of the 2nd Millennium BCE* (Harrassowitz, 2011).
12. D. Morandi Bonacossi, The creation of the Assyrian Heartland: New data from the "Land behind Nineveh," in *The Archaeology of Imperial Landscapes. A Comparative Study of Empires in the Ancient Near East and Mediterranean World*, B. S. Düring, T. Stek, Eds. (Cambridge Univ. Press, 2018), pp. 48–85.
13. T. J. Wilkinson, J. Ur, E. B. Wilkinson, M. Altaawe, Landscape and settlement in the Neo-Assyrian Empire. *Bull. Am. Sch. Orient. Res.* **340**, 23–56 (2005).
14. A. Kuhrt, The Assyrian heartland in the Achaemenid period. *Pallas* **43**, 239–254 (1995).
15. I. N. Medvedskaya, *Ancient Iran on the Eve of Empires (IX–VI century B.C.): The History of the Median Kingdom* (Petersburg Orientalism, St. Petersburg, 2010).
16. A. W. Schneider, S. F. Adali, "No harvest was reaped": Demographic and climatic factors in the decline of the Neo-Assyrian Empire. *Clim. Change* **127**, 435–446 (2014).
17. M. Hoerling, J. Eischeid, J. Perlwitz, X. Quan, T. Zhang, P. Pegion, On the increased frequency of Mediterranean drought. *J. Climate* **25**, 2146–2161 (2012).
18. C. P. Kelley, S. Mohtadi, M. A. Cane, R. Seager, Y. Kushnir, Climate change in the Fertile Crescent and implications of the recent Syrian drought. *Proc. Natl. Acad. Sci. U.S.A.* **112**, 3241–3246 (2015).
19. R. M. Trigo, C. M. Gouveia, D. Barriopedro, The intense 2007–2009 drought in the Fertile Crescent: Impacts and associated atmospheric circulation. *Agric. For. Meteorol.* **150**, 1245–1257 (2010).
20. L. Eklund, D. Thompson, Differences in resource management affects drought vulnerability across the borders between Iraq, Syria, and Turkey. *Ecol. Soc.* **22**, 9 (2017).
21. P. Flohr, D. Fleitmann, E. Zorita, A. Sadekov, H. Cheng, M. Bosomworth, L. Edwards, W. Matthews, R. Matthews, Late Holocene droughts in the Fertile Crescent recorded in a speleothem from northern Iraq. *Geophys. Res. Lett.* **44**, 1528–1536 (2017).
22. H. Cheng, A. Sinha, S. Verheyden, F. H. Nader, X. L. Li, P. Z. Zhang, J. J. Yin, L. Yi, Y. B. Peng, Z. G. Rao, Y. F. Ning, R. L. Edwards, The climate variability in northern Levant over the past 20,000 years. *Geophys. Res. Lett.* **42**, 8641–8650 (2015).
23. J. Gat, I. Carmi, Evolution of the isotopic composition of atmospheric waters in the Mediterranean Sea area. *J. Geophys. Res.* **75**, 3039–3048 (1970).
24. E. Bard, G. Delaygue, F. Rostek, F. Antonioli, S. Silenzi, D. P. Schrag, Hydrological conditions over the western Mediterranean basin during the deposition of the cold Sapropel 6 (ca. 175 kyr BP). *Earth Planet. Sci. Lett.* **202**, 481–494 (2002).
25. Y. Goldsmith, P. J. Polissar, A. Ayalon, M. Bar-Matthews, W. S. Broecker, The modern and Last Glacial Maximum hydrological cycles of the Eastern Mediterranean and the Levant from a water isotope perspective. *Earth Planet. Sci. Lett.* **457**, 302–312 (2017).
26. M. Werner, P. M. Langebroek, T. Carlsen, M. Herold, G. Lohmann, Stable water isotopes in the ECHAM5 general circulation model: Toward high-resolution isotope modeling on a global scale. *J. Geophys. Res. Atmos.* **116**, D15109 (2011).
27. J. E. Reade, Assyrian eponyms, kings and pretenders, 648–605 BC. *Orientalia* **67**, 255–265 (1998).
28. H. Wanner, L. Mercolli, M. Grosjean, S. P. Ritz, Holocene climate variability and change: A data-based review. *J. Geol. Soc. London* **172**, 254–263 (2015).
29. L. R. Stevens, H. E. Wright Jr., E. Ito, Proposed changes in seasonality of climate during the Lateglacial and Holocene at Lake Zeribar, Iran. *Holocene* **11**, 747–755 (2001).
30. L. R. Stevens, E. Ito, A. Schwab, H. E. Wright Jr., Timing of atmospheric precipitation in the Zagros Mountains inferred from a multi-proxy record from Lake Mirabad, Iran. *Quatern. Res.* **66**, 494–500 (2006).
31. A. Sharifi, A. Pourmand, E. A. Canuel, E. Ferer-Tyler, L. C. Peterson, B. Aichner, S. J. Feakins, T. Daryae, M. Djamali, A. N. Beni, H. A. K. Lahijani, P. K. Swart, Abrupt climate variability since the last deglaciation based on a high-resolution, multi-proxy peat record from NW Iran: The hand that rocked the Cradle of Civilization? *Quat. Sci. Rev.* **123**, 215–230 (2015).
32. B. Schilman, M. Bar-Matthews, A. Almogi-Labin, B. Luz, Global climate instability reflected by Eastern Mediterranean marine records during the late Holocene. *Palaeogeogr. Palaeoclimatol. Palaeoecol.* **176**, 157–176 (2001).
33. M. Bar-Matthews, A. Ayalon, M. Gilmour, A. Matthews, C. J. Hawkesworth, Sea–land oxygen isotopic relationships from planktonic foraminifera and speleothems in the Eastern Mediterranean region and their implication for paleorainfall during interglacial intervals. *Geochim. Cosmochim. Acta* **67**, 3181–3199 (2003).
34. M. Djamali, J. L. De Beaulieu, N. F. Miller, V. Andrieu-Ponel, P. Ponel, R. Lak, N. Sadeddin, H. Akhiani, H. Fazeli, Vegetation history of the SE section of the Zagros Mountains during the last five millennia; A pollen record from the Maharlou Lake, Fars Province, Iran. *Veg. Hist. Archaeobot.* **18**, 123–136 (2009).
35. F. B. Şimşek, M. N. Çağatay, Late Holocene high resolution multi-proxy climate and environmental records from Lake Van, eastern Turkey. *Quat. Int.* **486**, 57–72 (2018).
36. C. Kuzucuoğlu, W. Dörfler, S. Kunesch, F. Goupille, Mid- to late-Holocene climate change in central Turkey: The Tecer Lake record. *Holocene* **21**, 173–188 (2011).
37. U. B. Ulgen, S. O. Franz, D. Billekin, M. N. Çağatay, P. A. Roeser, L. Doner, J. Thein, Climatic and environmental evolution of Lake Iznik (NW Turkey) over the last ~ 4700 years. *Quat. Int.* **274**, 88–101 (2012).
38. J. N. Postgate, The economic structure of the Assyrian Empire, in *Power and Propaganda: A Symposium on Ancient Empires*, M. T. Larsen, Ed. (Akademisk Forlag, 1979), pp. 193–221.
39. L. Guanter, Y. Zhang, M. Jung, J. Joiner, M. Voigt, J. A. Berry, C. Fankenberg, A. R. Huete, P. Zarco-Tejada, J. Lee, M. S. Moran, G. Ponce-Campos, C. Beer, G. Camps-Valls, N. Buchmann, D. Gianelle, K. Klumpp, A. Cescatti, J. M. Baker, T. J. Griffis, Global and time-resolved monitoring of crop photosynthesis with chlorophyll fluorescence. *Proc. Natl. Acad. Sci. U.S.A.* **111**, E1327–E1333 (2014).
40. J. E. Curtis, The Assyrian heartland in the period 612–539 BC, in *Continuity of Empire: Assyria, Media, Persia*, G. B. Lanfranchi, M. Roaf, R. Rollinger, Eds. (Sargon Editrice e Libreria, 2003), pp. 157–172.
41. J. Keppner, The aftermath of the Assyrian empire as seen from the 'Red House' operation in Tell Sheikh Hamad (ancient Dur-Katlimmu), in *The Provincial Archaeology of the Assyrian Empire*, J. MacGinnis, D. Wicke, T. Greenfield, Eds. (Cambridge, McDonald Institute for Archaeological Research, 2016), pp. 177–187.
42. D. Morandi Bonacossi, Betrachtungen zur Siedlungs- und Bevölkerungsstruktur des Unteren Håbår-Gebietes in der neuassyrischen Zeit, in *Umwelt und Subsistenz der assyrischen Stadt Dür-Katlimmu am Unteren Håbår (Syrien)*, H. Kuhne, Ed. (Harrassowitz, 2008), pp. 189–214.
43. S. R. Hauser, Post-imperial Assyria, in *A Companion to Assyria*, E. Frahm, Ed. (John Wiley & Sons, 2017), pp. 229–246.
44. R. L. Edwards, J. Chen, G. J. Wasserburg, <sup>238</sup>U–<sup>234</sup>U–<sup>230</sup>Th–<sup>232</sup>Th systematics and the precise measurement of time over the past 500,000 years. *Earth Planet. Sci. Lett.* **81**, 175–192 (1987).
45. H. Cheng, R. L. Edwards, C.-C. Shen, V. J. Polyak, Y. Asmerom, J. Woodhead, J. Hellstrom, Y. Wang, X. Kong, C. Spötl, X. Wang, E. C. Alexander Jr., Improvements in <sup>230</sup>Th dating, <sup>230</sup>Th and <sup>234</sup>U half-life values, and U–Th isotopic measurements by multi-collector inductively coupled plasma mass spectrometry. *Earth Planet. Sci. Lett.* **371**, 82–91 (2013).
46. S. F. M. Breitenbach, K. Rehfeld, B. Goswami, J. U. L. Baldini, H. E. Ridley, D. J. Kennett, K. M. Prufer, V. V. Aquino, Y. Asmerom, V. J. Polyak, H. Cheng, J. Kurths, N. Marwan, COnstructing Proxy Records from Age models (COPRA). *Clim. Past* **8**, 1765–1779 (2012).
47. J. Haslett, A. Parnell, A simple monotone process with application to radiocarbon-dated depth chronologies. *J. R. Stat. Soc. C Appl.* **57**, 399–418 (2008).
48. C. B. Ramsey, S. Lee, Recent and planned developments of the program OxCal. *Radiocarbon* **55**, 720–730 (2013).
49. M. Mudelsee, *Climate Time Series Analysis: Classical Statistical and Bootstrap Methods* (Springer, 2010).
50. M. Ghil, M. R. Allen, M. D. Dettinger, K. Ide, D. Kondrashov, M. E. Mann, A. W. Robertson, A. Saunders, Y. Tian, F. Varadi, P. Yiou, Advanced spectral methods for climatic time series. *Rev. Geophys.* **40**, 3–1–3–41 (2002).
51. S. A. Salman, S. Shahid, T. Ismail, A. M. Al-Abadi, X.-j. Wang, E.-S. Chung, Selection of gridded precipitation data for Iraq using compromise programming. *Measurement* **132**, 87–98 (2019).
52. U. Schneider, A. Becker, P. Finger, A. Meyer-Christoffer, B. Rudolf, M. Ziese, *GPCC Full Data Reanalysis Version 7.0: Monthly Land-Surface Precipitation from Rain Gauges Built on GTS Based and Historic Data* (Research Data Archive at the National Center for Atmospheric Research, Computational and Information Systems Laboratory, 2016); <https://rda.ucar.edu/datasets/ds496.0/>.
53. I. Harris, P. D. Jones, T. J. Osborn, D. H. Lister, Updated high-resolution grids of monthly climatic observations—the CRU TS3. 10 Dataset. *Int. J. Climatol.* **34**, 623–642 (2014).
54. J. Joiner, L. Guanter, R. Lindstrot, M. Voigt, A. P. Vasilkov, E. M. Middleton, K. F. Huemrrich, Y. Yoshida, C. Frankenberg, Global monitoring of terrestrial chlorophyll fluorescence from moderate-spectral-resolution near-infrared satellite measurements: Methodology, simulations, and application to GOME-2. *Atmos. Meas. Tech.* **6**, 2803–2823 (2013).
55. C. H. Hendy, A. T. Wilson, Palaeoclimatic data from speleothems. *Nature* **216**, 48–51 (1968).
56. J. A. Dorale, Z. Liu, Limitations of Hendy test criteria in judging the paleoclimatic suitability of speleothems and the need for replication. *J. Cave Karst Stud.* **71**, 73–80 (2009).
57. J. A. Fohlmeister, A statistical approach to construct composite climate records of dated archives. *Quat. Geochronol.* **14**, 48–56 (2012).
58. N. J. Steiger, E. J. Steig, S. G. Dee, G. H. Roe, G. J. Hakim, Climate reconstruction using data assimilation of water isotope ratios from ice cores. *J. Geophys. Res. Atmos.* **122**, 1545–1568 (2017).
59. K. K. Ali, Q. Y. Al-Kubaisi, K. B. Al-Paruany, Isotopic study of water resources in a semi-arid region, western Iraq. *Environ. Earth Sci.* **74**, 1671–1686 (2015).
60. Z. Kattan, Chemical and environmental isotope study of precipitation in Syria. *J. Arid Environ.* **35**, 601–615 (1997).
61. J. Neumann, S. Parpola, Climatic change and the eleventh-century eclipse of Assyria and Babylonia. *J. Near East. Stud.* **46**, 161–182 (1987).

62. D. Kaniewski, E. Van Campo, J. Guiot, S. Le Burel, T. Otto, C. Baeteman, Environmental roots of the late bronze age crisis. *PLOS ONE* **8**, e71004 (2013).
63. K. Radner, *Ancient Assyria: A Very Short Introduction* (Oxford Univ. Press, 2015).
64. D. Khan, Taharqa, King of Kush and the Assyrians. *J. Soc. Study Egypt. Antiq.* **31**, 109–128 (2004).
65. A. Kuhrt, *The Ancient Near East, c. 3000–320 BC* (Routledge, New York and London, 1995).
66. K. Deller, Getreidekursangaben in neuassyrischen Rechtsurkunden. *Orientalia* **33**, 257–261 (1964).
67. D. Morandi Bonacossi, Water for Nineveh. The Nineveh Irrigation System in the regional context of the 'Assyrian Triangle': A first geoarchaeological assessment, in *Water for Assyria, Studia Chaburensia*, H. Kühne, Ed. (Harrassowitz, 2018), vol. 7, pp. 77–115.
68. J. Ur, J. Reade, The hydraulic landscape of Nimrud. *Mesopotamia* **50**, 25–51 (2015).
69. A. Millard, *The Eponyms of the Neo-Assyrian Empire, 910–612 BC State Archives of Assyria Studies, vol. II*, (Helsinki, Helsinki University Press, 1994).
70. H. C. Rawlinson, The Assyrian canon verified by the record of a solar eclipse, B.C. 763. *Athenaeum* **2064**, 660–661 (1867).
71. H. Hunger, Zur datierung der neuassyrischen Eponymenlisten. *Altorientalischen Forschungen* **35**, 323–325 (2008).
72. S. Parpola, *Letters from Assyrian scholars to the Kings Esarhaddon and Assurbanipal. Part II: Commentary and appendices* (Kevelaer, Verlag Butzon und Bercker, Alter Orient und Altes Testament, Bd. 5/2, 1983).
73. Z. Stevanović, A. Lurkiewicz, A. Maran, New insights into karst and caves of Northwestern Zagros (Northern Iraq). *Acta Carsologica* **38**, 83–96 (2009).
74. M. Laumanns, A. Rasch, A. Audra, *Karst and Caves of Iraq (Including the Results of a 2007 Kurdish-German Speleological Project and an Overview on Hypogenic Sulphidic Speleogenesis)*. (Berliner Höhlenkundliche Berichte, 2008) vol. 26.
75. I. Friedman, J. R. O'Neil, Compilation of the isotope fractionation factors of geochemical interest, in *Data of Geochemistry*, M. Fleischer, Ed. (U.S. Geological Survey Professional Paper, 1977), pp. 1–12.
76. S.-T. Kim, J. R. O'Neil, Equilibrium and nonequilibrium oxygen isotope effects in synthetic carbonates. *Geochim. Cosmochim. Acta* **61**, 3461–3475 (1997).
77. A. Demeny, S. Kele, Z. Siklosy, Empirical equations for the temperature dependence of calcite-water oxygen isotope fractionation from 10 to 70° C. *Rapid Commun. Mass Spectrom.* **24**, 3521–3526 (2010).
78. D. M. Tremaine, P. N. Froelich, Y. Wang, Speleothem calcite farmed in situ: Modern calibration of  $\delta^{18}\text{O}$  and  $\delta^{13}\text{C}$  paleoclimate proxies in a continuously-monitored natural cave system. *Geochim. Cosmochim. Acta* **75**, 4929–4950 (2011).
79. T. B. Coplen, Calibration of the calcite–water oxygen-isotope geothermometer at Devils Hole, Nevada, a natural laboratory. *Geochim. Cosmochim. Acta* **71**, 3948–3957 (2007).

**Acknowledgments:** We thank A. Bachmann and members of “Nature Iraq” for their help with the cave monitoring, sample collection, and field planning; M. Muhammed for collecting precipitation samples; and M. Rincon for the isotope laboratory analysis. We thank J. Ur for constructive comments on an earlier version of this manuscript. **Funding:** This work was supported by the Natural Science Foundation of China (grants 41888101 and 41731174 to H.C. and grant 41703007 to G.K.) and the National Science Foundation (grant 0823554 to A.S., grant 1502776 to M.B., grant 1702816 to R.L.E. and H.C., and grant 1049219 to L.D.S.). **Author contributions:** A.S., H.W., and A.W.S. wrote the first draft. J.R., L.D.S., and A.S. conducted the stable isotope measurements. H.C., G.K., and R.L.E. conducted the radiometric dating. A.S., G.K., and H.L. performed the statistical analysis. M.B. conducted the SIF analysis. All authors discussed the results and provided input on the manuscript. **Competing interests:** The authors declare that they have no competing interests. **Data and materials availability:** All data are available in the main text and/or the Supplementary Materials and will be archived at the National Climatic Data Center (<https://ncdc.noaa.gov/>). Request for materials should be addressed to A.S. (asinha@csudh.edu).

Submitted 11 April 2019  
Accepted 17 September 2019  
Published 13 November 2019  
10.1126/sciadv.aax6656

**Citation:** A. Sinha, G. Kathayat, H. Weiss, H. Li, H. Cheng, J. Reuter, A. W. Schneider, M. Berkelhammer, S. F. Adali, L. D. Stott, R. L. Edwards, Role of climate in the rise and fall of the Neo-Assyrian Empire. *Sci. Adv.* **5**, eaax6656 (2019).

## Role of climate in the rise and fall of the Neo-Assyrian Empire

Ashish Sinha, Gayatri Kathayat, Harvey Weiss, Hanying Li, Hai Cheng, Justin Reuter, Adam W. Schneider, Max Berkelhammer, Selim F. Adali, Lowell D. Stott and R. Lawrence Edwards

*Sci Adv* 5 (11), eaax6656.  
DOI: 10.1126/sciadv.aax6656

ARTICLE TOOLS	<a href="http://advances.sciencemag.org/content/5/11/eaax6656">http://advances.sciencemag.org/content/5/11/eaax6656</a>
SUPPLEMENTARY MATERIALS	<a href="http://advances.sciencemag.org/content/suppl/2019/11/08/5.11.eaax6656.DC1">http://advances.sciencemag.org/content/suppl/2019/11/08/5.11.eaax6656.DC1</a>
REFERENCES	This article cites 54 articles, 2 of which you can access for free <a href="http://advances.sciencemag.org/content/5/11/eaax6656#BIBL">http://advances.sciencemag.org/content/5/11/eaax6656#BIBL</a>
PERMISSIONS	<a href="http://www.sciencemag.org/help/reprints-and-permissions">http://www.sciencemag.org/help/reprints-and-permissions</a>

Use of this article is subject to the [Terms of Service](#)

---

*Science Advances* (ISSN 2375-2548) is published by the American Association for the Advancement of Science, 1200 New York Avenue NW, Washington, DC 20005. The title *Science Advances* is a registered trademark of AAAS.

Copyright © 2019 The Authors, some rights reserved; exclusive licensee American Association for the Advancement of Science. No claim to original U.S. Government Works. Distributed under a Creative Commons Attribution NonCommercial License 4.0 (CC BY-NC).